Enhancing the Coherence of Superconducting Quantum Bits with Electric Fields

Jürgen Lisenfeld,*) Alexander Bilmes, and Alexey V. Ustinov
Physikalisches Institut, Karlsruhe Institute of Technology, 76131 Karlsruhe, Germany

(Dated: 3 August 2022)

In the endeavour to make quantum computers a reality, integrated superconducting circuits have become a promising architecture. A major challenge of this approach is decoherence originating from spurious atomic tunneling defects at the interfaces of qubit electrodes, which may resonantly absorb energy from the qubit's oscillating electric field and reduce the qubit's energy relaxation time T_1. Here, we show that qubit coherence can be improved by tuning dominating defects away from the qubit resonance using an applied DC-electric field. We demonstrate a method that optimizes the applied field bias and enhances the average qubit T_1 time by 23%. We also discuss how local gate electrodes can be implemented in superconducting quantum processors to enable simultaneous in-situ coherence optimization of individual qubits.

INTRODUCTION

Superconducting integrated circuits have evolved into a powerful architecture for creating artificial quantum systems. In state-of-the-art experiments, tens of qubits are coherently operated as quantum simulators and universal processors[1–4] while access to prototype devices is being offered via the cloud to accelerate the development of practical quantum algorithms[5]. On the way forward, mitigating decoherence is one of the central challenges, because it hinders further up-scaling and implementation of quantum error correction[6,7].

Today's processors typically employ transmon qubits that are based on discrete energy levels in non-linear LC-resonators formed by a capacitively shunted Josephson junction[8]. A large part of decoherence in such qubits is due to dielectric loss in the native surface oxides of the capacitor electrodes[9,10]. This loss shows a remarkably structured frequency dependence[11,12] which originates in the individual resonances of spurious atomic tunneling defects[13]. These defects form a sparse bath of parasitic two-level quantum systems, so-called TLS, which have been evoked long ago to explain the anomalous low-temperature properties of amorphous materials[14,15].When a TLS has an electric dipole moment, it may resonantly absorb energy from the oscillating electric field of the qubit mode, and efficiently dissipate it into the phonon-[16] or BCS quasiparticle bath[17]. Moreover, TLS' resonance frequency may fluctuate in time due to interactions with thermally activated, randomly switching low-energy TLS[18–22]. This mechanism efficiently transforms thermal noise into the qubit's environmental spectrum, and causes fluctuations of the qubit's resonance frequency and energy relaxation rate T_1[23–25]. For quantum processors, this implies fluctuations of their quantum volume (i.e. computational power)[26].

Recently, we have shown that the resonance frequencies of TLS located on thin-film electrodes and the substrate of a qubit circuit can be tuned by an applied DC-electric field[10,27]. Accordingly, it becomes possible to tune defects that dominate qubit energy relaxation away from the qubit resonance, and this results in longer relaxation times T_1. Here, we demonstrate this concept using a simple routine which maximizes the T_1 time of a qubit by searching for an optimal electric field bias. The method was tested at various qubit resonance frequencies and increased the qubit T_1 time on average by 23%.

ELECTRIC FIELD TUNING OF TLS

For our experiments, we fabricated a transmon qubit sample in the so-called 'X-Mon' design following Barends et al.[12] as shown in Fig. 1**b**. The flux-tunable qubit uses a submicron-sized Al/AlOx/Al tunnel junction made by shadow evaporation as described in detail in Ref.[28]. The electric field for TLS tuning is generated by a DC-electrode installed on the lid of the sample housing ≈ 0.9 mm above the qubit chip's surface as illustrated in Fig. 1**a**. The electrode is made from a copper foil that is insulated by Kapton foil from the housing. To improve E-field homogeneity in vicinity of the qubits, the electrode has a comparable size than the qubit chip. More details on this setup are described in Ref.[10].

The response of TLS to the applied electric field is observed by measuring the qubit energy relaxation time T_1 as a function of qubit frequency, which shows Lorentzian minima whenever sufficiently strongly interacting TLS are tuned into resonance. A detailed view on the rich TLS spectrum as shown in Fig. 1**d** is obtained using swap-spectroscopy[29]. With this protocol, TLS are detected by the resonant reduction of the qubit's excited state population after it was tuned for a fixed time interval to various probing frequencies. In the studied sample, only a single TLS was observed that did not couple to the applied E-field, indicating that it was likely residing in a tunnel barrier of the submicron-sized qubit junctions where no DC-electric field exists[8]. This confirms that only a few resonant TLS are typically found in small area Josephson junctions[6,28,30], and dielectric loss is dominated by defects on the interfaces of the qubit electrodes[9,10,27]. This is true as long as qubits are fabricated with methods[31–33] that avoid the formation of large-area stray Josephson junctions which are known to contribute many additional defects[10,28].

In Fig. 1**d**, some TLS are observed whose resonance frequencies show strong fluctuations or telegraphic switching

*)Corresponding author: juergen.lisenfeld@kit.edu

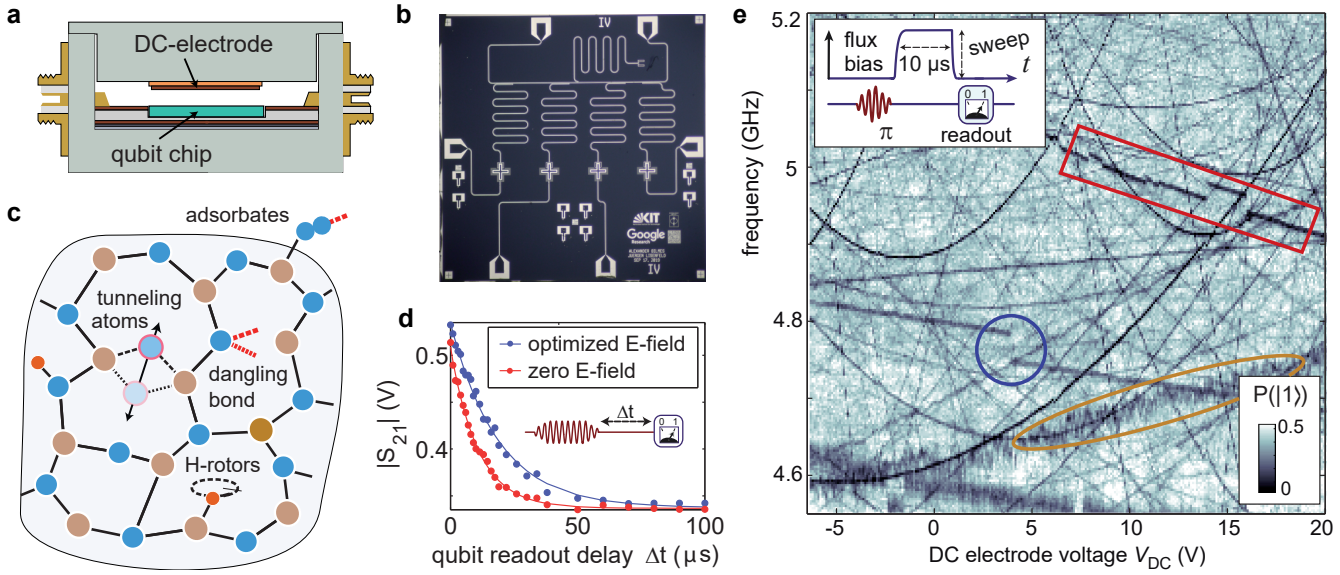

FIG. 1. **Tuning defects by an electric field. a** Cross-section through the sample housing. The electrode to generate the E-field consists of a Copper-Foil/Kapton Foil stack glued to the lid of the sample holder above the qubit chip, and voltage-biased against ground. **b** Photograph of the XMon qubit samples used in this work. **c** Illustration of defects which appear in the amorphous oxides of qubit electrodes. **d** Exemplary measurements of the decaying qubit population after a long exciting microwave pulse (see inset) to determine the T_1 time. Red (blue) points were acquired at zero (the optimized) applied E-field. **e** Resonances of individual TLS (dark traces), observed as accelerated decay of the qubit's excited state population (colour scale) using the swap-spectroscopy protocol shown in the inset. The circle marks coupling of a TLS to a metastable fluctuator which may cause hysteresis in E-field sweeps. Rectangle and ellipse indicate the fluctuating resonance frequencies of TLS coupled to slowly and quickly fluctuating thermal TLSs, respectively.

due to their interaction with low-energy TLS that are thermally activated. We note that TLS may also interact with classical bistable charge fluctuators that have a very small switching rate between their states. Since these fluctuators may also be tuned by the applied electric field, hysteresis effects may appear in electric field sweeps since the state of a fluctuator, and hereby the resonance frequency of a high-energy TLS, may depend on the history of applied E-fields[34]. An example of such an interacting TLS-fluctuator system is marked by the circle in Fig. 1**d**, where the resonance frequency of a TLS abruptly changed.

METHOD FOR OPTIMIZING THE QUBIT T_1 TIME

As it is evident from Fig. 1**d**, at each qubit operation frequency there is a preferable electric field bias where most of the dominating TLS are tuned out of qubit resonance and the T_1 time is maximized. In the following, we describe a simple routine by which an optimal E-field bias can be automatically determined.

First, the qubit T_1-time is measured for a range of applied electric fields. Hereby, the T_1-time is obtained from exponential fits to the decaying qubit population probability after it was excited by a microwave pulse, measured using the common protocol shown in the inset of Fig. 1**c**. Figure 2**a** shows the resulting electric field dependence of T_1 (black data points), measured at various qubit resonance frequencies (rows I to III). These data are then smoothed by a nearest-neighbour average (gray curve) to average out individual dips and peaks in order to amplify broader maxima that promise a more stable improvement.

Next, the E-field is set to the value where the maximum T_1-time occurred (blue circle in Fig. 2**a**). Hereby, it is recommended to approach the detected optimal E-field from the same value where the previous E-field sweep was started. This helps to avoid the mentioned hysteresis effects in the TLS resonance frequencies that may occur when they are coupled to meta-stable field-tunable TLS whose state depends on the history of applied E-fields. Finally, a second pass is performed, sweeping the E-field in finer steps around its previously determined optimum value until the obtained T_1 time is close to the maximum value that was observed in the previous sweep. This ensures that hysteresis effects are better compensated and the finer step helps to avoid sharp dips that were not resolved in the first pass. Data obtained in the second pass are plotted in green in Fig. 2**a**).

BENCHMARKING THE METHOD

To test the efficiency of the optimization routine, first the qubit T_1 is repeatedly observed during 30 minutes at zero applied electric field as a reference (red data in Fig. 2**b**). Afterwards, the optimization routine searches for the electric field which maximizes the qubit's coherence time by taking

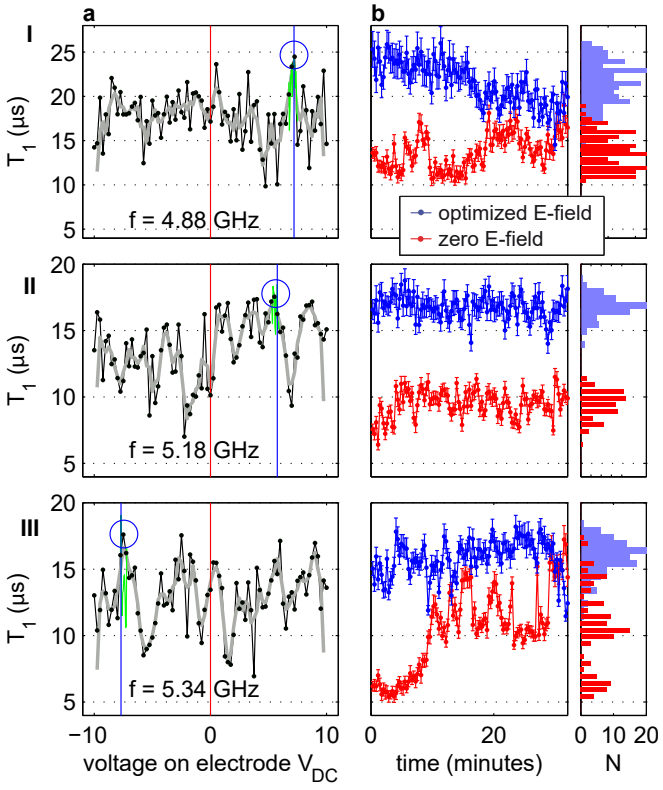

FIG. 2. **Benchmarking the optimization algorithm**. Rows **I** - **III** were taken at the indicated qubit operation frequencies. **a** Qubit T_1-time vs. applied electric field. Black data points are obtained from fits to exponential decay curves as shown in Fig. 1**c**. Dips in T_1 indicate the resonance with strongly coupled TLS. The gray curve is a 3-point nearest neighbour average, whose maximum (blue circle) is close to the determined optimum bias field. The green line indicates T_1 obtained in the second pass, sweeping the field in finer steps in a small range around the E-field of previously determined T_1 maximum. **b** Comparison of qubit T_1 times between an optimized E-field bias (blue data) vs. zero applied E-field (red data), measured as a function of time during 30 minutes.

data as shown in Fig. 2**a**. The result is then checked by monitoring the T_1-time at the found optimal E-field during another 30 minutes (blue data in Fig. 2**b**). Evidently, during most of this time, acquired T_1 times after optimization are higher than the reference values that were obtained at zero applied electric field.

To measure the average improvement of the optimization routine, the benchmarking protocol was repeated at various (in total 59) qubit resonance frequencies, see the Supplementary Material for the full data set. Figures 3**a** and **b** summarize the absolute and relative improvement of the qubit T_1-time at all investigated qubit resonance frequencies. In most cases (85%), the routine improved the 30-minute average qubit T_1-time. The improvement was larger than 10% T_1 in 67% of cases, and enhanced T_1 by more than 20% in 46% of all tries. Averaged over all tested qubit resonance frequencies, the T_1 time improvement was $\approx 23\%$.

To check how much the optimization routine affects the temporal fluctuation strength of the qubit's T_1 time, the standard deviation of observed T_1 times during the 30 minute intervals before and after optimization were compared. The result is shown in Figure 3**c**. In slightly more than half cases (59%), the T_1 time fluctuations increased after optimization. This might be mitigated by enhancing the optimization algorithm such that it prefers broader T_1-time peaks which are less sensitive to TLS frequency fluctuations, and by including the T_1 fluctuation strength at detected peaks as a criterion.

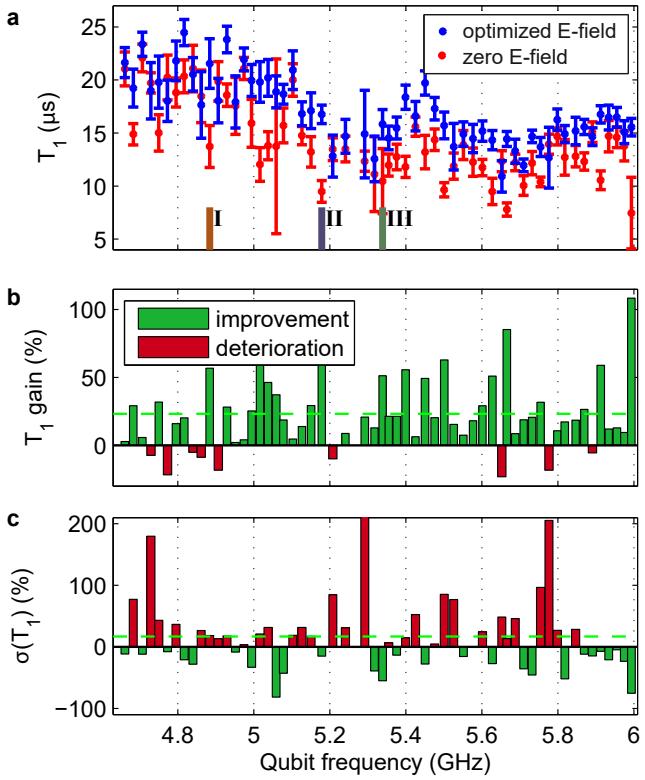

FIG. 3. **Results. a)** Qubit T_1 times after E-field optimization (blue data) and at zero applied E-field (red data), tested at various qubit frequencies and averaged over 30 minutes. The error bars indicate the spread (standard deviation) of T_1 over 30 minutes. **b)** Relative improvement of qubit T_1 after optimization. In a few cases, the routine results in a smaller T_1 time (red bars). Best and average T_1-time improvements are 108% and 23.2%, respectively. **c)** Fluctuations of T_1-times (standard deviation over 30 minutes). On average, the fluctuations were 17% higher for the optimized E-field.

INTEGRATION WITH QUANTUM PROCESSORS

When each qubit in a processor is coupled to a dedicated local gate electrode, the optimization routine can be applied simultaneously on all qubits. This tuneup-process is facilitated when no cross-talk of a gate electrode to neighboring qubits occurs. Moreover, the generated electric field should be sufficiently strong all along the edges of the qubit island and the opposing ground plane (where surface defects are most strongly coupled to the qubit[10]), so that all relevant

TLS can be tuned by $\delta\varepsilon \gtrsim 100$ MHz to decouple them from the qubit. Assuming a relatively small coupling TLS dipole moment component of $p = 0.1\,\text{eÅ}$[10,11,35], this corresponds to required field strengths $E = \delta\varepsilon/p \approx 40\,\text{kV/m}$. Given a typical distance between the DC-electrode and the qubit electrodes of below 1 mm, such E-fields are unproblematically obtained with a bias voltage of a few Volt on the DC-electrode.

Figure 4 shows a possible implementation of a gate electrode array, which is located on a separate wiring chip that is bumb-bonded to the chip carrying the qubits in a flip-chip configuration[36,37]. In Fig. 4**a**, a top view of two Xmon-type[12] qubits is shown, where the gate electrode above the left qubit is indicated in orange. The electrode extends slightly over the edges of the qubit island's opposing ground plane to ensure the tunability of TLS in this region.

The cross section of the chip stack is sketched in Fig. 4 **b**, showing that the gate electrodes are separated from the ground plane of the wiring chip by a thin film insulator.
The simulated electric field strength in this region is drawn to-scale in Fig. 4**c**, for the case when the left electrode is biased at 1 V while all other metallic parts (including the qubit island [10]) are kept at zero potential. As expected, the induced field strength decays on a length scale of roughly the distance between the two chips, given that qubits are surrounded by a ground plane and also the wiring chip has a ground plane. For a qubit-to-qubit separation of $d > 100\,\mu$m as used in the presented simulation, we accordingly find the cross-talk to be below 10^{-4}.

Alternatively, the local electrodes could also be placed on the backside of the qubit chip. In this case, the substrate thickness will determine the horizontal field screening length, and stronger cross-talk can be expected. However, FEM simulations of the induced E-fields in a given processor layout should allow one to sufficiently compensate for this cross-talk.

In principle, it is also possible to implement our method by tuning the resonance frequencies of TLS by applied mechanical strain[29,38]. However, it will be difficult to control the local strain for each qubit on a processor chip independently.

CONCLUSION

We present an experimental setup and an automatic routine that extends the energy relaxation time T_1 of superconducting transmon qubits. The idea is to expose the qubit electrodes to a DC-electric field at which the most detrimental TLS-defects are tuned out of qubit resonance. Averaging over qubit working frequencies and a 30-minute time interval (that was limited by time constraints), the T_1-time was improved by 23% compared to zero applied electric field.

The benefit of the optimization may decrease or vanish with time due to TLS resonance frequency fluctuations. However, recent experiments[22] suggests that the frequency shifts of TLS remain smaller than 10 MHz during 10 days of measurement, which is also corroborated by the notion that each TLS can only interact with a limited number of thermally active defects in its vicinity[18,39,40]. This suggests

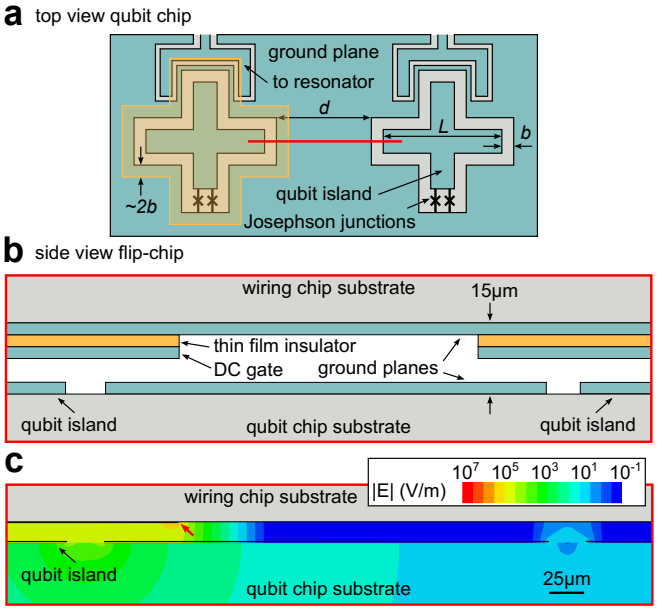

FIG. 4. **a** Top view sketch of two Xmon-qubits. The orange region indicates the gate electrode above the left qubit. **b** Cross-section of the flip-chip stack, sketched along the red line shown in **a**. The DC gate electrodes are separated by thin-film insulators from the wiring chip's ground plane. **c** Simulated electric field strength when 1 V is applied to the left gate electrode. The field decays horizontally on a scale of about the distance between the qubit and the wiring chips (here, 15 μm), resulting in small cross-talk below 10^{-4}.

that our optimization routine can be further improved when it is repeatedly executed during several hours or days, in order to identify an electric field bias that protects the qubit on long timescales from interactions with strongly coupled TLS.

In our experiments, the optimization routine took less than 10 minutes (to acquire about 60 values of qubit T_1 at several E-fields). However, the data shown in Fig. 2**a** suggests that the range of applied E-fields may be reduced, which together with further optimizations such as less averaging in individual T_1-time measurements, may reduce the optimization time to below 2 or 3 minutes.

Analysis of the raw data such as shown in Fig. 2 and the Supplementary Material suggests that more stable improvements might be achieved by improving the algorithm, e.g. by including the width of a peak in T_1 vs. E-field as a criterion next to the height of the peak. Moreover, we expect that deterioration of the 30-minute average qubit T_1 time by the optimization routine, as it occurred in a few ($\approx$ 15%) cases in these tests, can be avoided by averaging over several E-field sweeps to better account for TLS showing strong resonance frequency fluctuations. Also, one may devise a feedback mechanism that regularly readjusts the E-field bias on the basis of qubit error rates obtained during quantum algorithms.

The ability to tune TLS out of resonance with a qubit is especially beneficial for processors implementing fixed-frequency qubits, which can be tuned only in a limited range

by exploiting the AC-stark shift[41]. This may still allow one to improve qubit coherence by evading strongly coupled TLS as it was recently demonstrated by Zhao et al.[42]. However, even when tunable qubits are used, it is still necessary to mutually balance their individual resonance frequencies to avoid crosstalk and to maximize gate fidelities, and this will be greatly simplified if qubit coherence can be optimized at all frequencies by having independent control of the TLS bath. Also, to improve two-qubit gates that require qubit frequency excursions, one could adjust our optimization procedure to minimize the number of TLS that have resonances in the traversed frequency interval.

Our simulations indicated that it is straight-forward to equip each qubit in a processor with local gate electrodes, which will allow one to simultaneously improve T_1 of all qubits. We thus see good opportunities for this technique to become a standard in superconducting quantum processors.

METHODS

The qubit sample is a stray-junction free transmon qubit that was fabricated by A. Bilmes as described in detail in Ref.[28]. For details about the experimental setup, the implementation of the DC-electrode for defect tuning, and simulations of the electric field, we refer to Ref.[10].

ACKNOWLEDGEMENTS

This work was funded by Google LLC which is gratefully acknowledged. JL thanks for funding from the Baden-Württemberg-Stiftung, and for funding from the Bundesministerium für Forschung und Bildung (BMBF) in the frame of the QSolid projekt. We acknowledge support by the KIT-Publication Fund of the Karlsruhe Institute of Technology.

AUTHOR CONTRIBUTION

JL devised and implemented idea and method, performed the experiments, and analyzed the data. AB built the qubit setup for E-field tuning, designed and fabricated the investigated qubits, and performed FEM simulations. The manuscript was written by JL with assistance from AB.

REFERENCES

[1] F. Arute, K. Arya, R. Babbush, D. Bacon, J. C. Bardin, R. Barends, R. Biswas, S. Boixo, F. G. Brandao, D. A. Buell, *et al.*, "Quantum supremacy using a programmable superconducting processor," Nature **574**, 505–510 (2019).

[2] P. Jurcevic, A. Javadi-Abhari, L. S. Bishop, I. Lauer, D. F. Bogorin, M. Brink, L. Capelluto, O. Günlük, T. Itoko, N. Kanazawa, *et al.*, "Demonstration of quantum volume 64 on a superconducting quantum computing system," Quantum Science and Technology **6**, 025020 (2021).

[3] J. Otterbach, R. Manenti, N. Alidoust, A. Bestwick, M. Block, B. Bloom, S. Caldwell, N. Didier, E. S. Fried, S. Hong, *et al.*, "Unsupervised machine learning on a hybrid quantum computer," arXiv preprint arXiv:1712.05771 (2017).

[4] Y. Wu, W.-S. Bao, S. Cao, F. Chen, M.-C. Chen, X. Chen, T.-H. Chung, H. Deng, Y. Du, D. Fan, *et al.*, "Strong quantum computational advantage using a superconducting quantum processor," Physical review letters **127**, 180501 (2021).

[5] S. Blinov, B. Wu, and C. Monroe, "Comparison of cloud-based ion trap and superconducting quantum computer architectures," AVS Quantum Science **3**, 033801 (2021).

[6] C. E. Murray, "Material matters in superconducting qubits," Materials Science and Engineering: R: Reports **146**, 100646 (2021).

[7] M. Kjaergaard, M. E. Schwartz, J. Braumüller, P. Krantz, J. I.-J. Wang, S. Gustavsson, and W. D. Oliver, "Superconducting qubits: Current state of play," arXiv preprint arXiv:1905.13641 (2019).

[8] J. Koch, M. Y. Terri, J. Gambetta, A. A. Houck, D. Schuster, J. Majer, A. Blais, M. H. Devoret, S. M. Girvin, and R. J. Schoelkopf, "Charge-insensitive qubit design derived from the cooper pair box," Physical Review A **76**, 042319 (2007).

[9] C. Wang, C. Axline, Y. Y. Gao, T. Brecht, Y. Chu, L. Frunzio, M. Devoret, and R. J. Schoelkopf, "Surface participation and dielectric loss in superconducting qubits," Applied Physics Letters **107**, 162601 (2015).

[10] J. Lisenfeld, A. Bilmes, A. Megrant, R. Barends, J. Kelly, P. Klimov, G. Weiss, J. M. Martinis, and A. V. Ustinov, "Electric field spectroscopy of material defects in transmon qubits," npj Quantum Information **5**, 1–6 (2019).

[11] J. M. Martinis, K. B. Cooper, R. McDermott, M. Steffen, M. Ansmann, K. D. Osborn, K. Cicak, S. Oh, D. P. Pappas, R. W. Simmonds, and C. C. Yu, "Decoherence in Josephson qubits from dielectric loss," Physical Review Letters **95**, 210503 (2005).

[12] R. Barends, J. Kelly, A. Megrant, D. Sank, E. Jeffrey, Y. Chen, Y. Yin, B. Chiaro, J. Mutus, C. Neill, P. O'Malley, P. Roushan, J. Wenner, T. C. White, A. N. Cleland, and J. M. Martinis, "Coherent josephson qubit suitable for scalable quantum integrated circuits," Phys. Rev. Lett. **111**, 080502 (2013).

[13] C. Müller, J. H. Cole, and J. Lisenfeld, "Towards understanding two-level-systems in amorphous solids: insights from quantum circuits," Reports on Progress in Physics **82**, 124501 (2019).

[14] W. A. Phillips, "Two-level states in glasses," Reports on Progress in Physics **50**, 1657 (1987).

[15] P. W. Anderson, B. I. Halperin, and C. M. Varma, "Anomalous low-temperature thermal properties of glasses and spin glasses," Philosophical Magazine **25**, 1–9 (1972).

[16] J. Jäckle, "On the ultrasonic attenuation in glasses at low temperatures," Zeitschrift für Physik A Hadrons and nuclei **257**, 212–223 (1972).

[17] A. Bilmes, S. Zanker, A. Heimes, M. Marthaler, G. Schön, G. Weiss, A. V. Ustinov, and J. Lisenfeld, "Electronic decoherence of two-level systems in a josephson junction," Physical review B **96**, 064504 (2017).

[18] J. L. Black and B. I. Halperin, "Spectral diffusion, phonon echoes, and saturation recovery in glasses at low temperatures," Phys. Rev. B **16**, 2879 (1977).

[19] P. V. Klimov, J. Kelly, Z. Chen, M. Neeley, A. Megrant, B. Burkett, R. Barends, K. Arya, B. Chiaro, Y. Chen, A. Dunsworth, A. Fowler, B. Foxen, C. Gidney, M. Giustina, R. Graff, T. Huang, E. Jeffrey, E. Lucero, J. Y. Mutus, O. Naaman, C. Neill, C. Quintana, P. Roushan, D. Sank, A. Vainsencher, J. Wenner, T. C. White, S. Boixo, R. Babbush, V. N. Smelyanskiy, H. Neven, and J. M. Martinis, "Fluctuations of energy-relaxation times in superconducting qubits," Phys. Rev. Lett. **121**, 090502 (2018).

[20] S. Schlör, J. Lisenfeld, C. Müller, A. Bilmes, A. Schneider, D. P. Pappas, A. V. Ustinov, and M. Weides, "Correlating decoherence in transmon qubits: Low frequency noise by single fluctuators," Phys. Rev. Lett. **123**, 190502 (2019).

[21] J. J. Burnett, A. Bengtsson, M. Scigliuzzo, D. Niepce, M. Kudra, P. Delsing, and J. Bylander, "Decoherence benchmarking of superconducting qubits," npj Quantum Information **5**, 54 (2019).

[22] M. Carroll, S. Rosenblatt, P. Jurcevic, I. Lauer, and A. Kandala, "Dynamics of superconducting qubit relaxation times," arXiv preprint arXiv:2105.15201 (2021).

[23] L. Faoro and L. B. Ioffe, "Internal Loss of Superconducting Resonators Induced by Interacting Two-Level Systems," Physical Review Letters **109**, 157005 (2012).

[24] C. Müller, J. Lisenfeld, A. Shnirman, and S. Poletto, "Interacting two-level defects as sources of fluctuating high-frequency noise in superconducting circuits," Phys. Rev. B **92**, 035442 (2015).

[25] J. Burnett, L. Faoro, I. Wisby, V. Gurtovoi, A. V. Chernykh, G. Mikhailov, V. Tulin, R. Shaikhaidarov, V. Antonov, P. Meeson, A. Y. Tzalenchuk, and T. Lindström, "Evidence for interacting two-level systems from the 1/f noise of a superconducting resonator," Nat. Commun. **5**, 4119 (2014).

[26] E. Pelofske, A. Bärtschi, and S. Eidenbenz, "Quantum volume in practice: What users can expect from nisq devices," arXiv preprint arXiv:2203.03816 (2022).

[27] A. Bilmes, A. Megrant, P. Klimov, G. Weiss, J. M. Martinis, A. V. Ustinov, and J. Lisenfeld, "Resolving the positions of defects in superconducting quantum bits," Scientific Reports **10**, 1–6 (2020).

[28] A. Bilmes, S. Volosheniuk, A. V. Ustinov, and J. Lisenfeld, "Probing defect densities at the edges and inside josephson junctions of superconducting qubits," npj Quantum Information **8**, 1–6 (2022).

[29] J. Lisenfeld, G. J. Grabovskij, C. Müller, J. H. Cole, G. Weiss, and A. V. Ustinov, "Observation of directly interacting coherent two-level systems in an amorphous material," Nat Commun **6**, 6182 (2015).

[30] Z. Kim, V. Zaretskey, Y. Yoon, J. Schneiderman, M. Shaw, P. Echternach, F. Wellstood, and B. Palmer, "Anomalous avoided level crossings in a cooper-pair box spectrum," Physical Review B **78**, 144506 (2008).

[31] A. Dunsworth, A. Megrant, C. Quintana, Z. Chen, R. Barends, B. Burkett, B. Foxen, Y. Chen, B. Chiaro, A. Fowler, *et al.*, "Characterization and reduction of capacitive loss induced by sub-micron josephson junction fabrication in superconducting qubits," Applied Physics Letters **111**, 022601 (2017).

[32] A. Osman, J. Simon, A. Bengtsson, S. Kosen, P. Krantz, D. P. Lozano, M. Scigliuzzo, P. Delsing, J. Bylander, and A. Fadavi Roudsari, "Simplified josephson-junction fabrication process for reproducibly high-performance superconducting qubits," Applied Physics Letters **118**, 064002 (2021).

[33] A. Bilmes, A. K. Händel, S. Volosheniuk, A. V. Ustinov, and J. Lisenfeld, "In-situ bandaged josephson junctions for superconducting quantum processors," Superconductor Science and Technology **34**, 125011 (2021).

[34] S. M. Meißner, A. Seiler, J. Lisenfeld, A. V. Ustinov, and G. Weiss, "Probing individual tunneling fluctuators with coherently controlled tunneling systems," Physical Review B **97**, 180505 (2018).

[35] C.-C. Hung, L. Yu, N. Foroozani, S. Fritz, D. Gerthsen, and K. D. Osborn, "Probing hundreds of individual quantum defects in polycrystalline and amorphous alumina," Physical Review Applied **17**, 034025 (2022).

[36] B. Foxen, J. Y. Mutus, E. Lucero, R. Graff, A. Megrant, Y. Chen, C. Quintana, B. Burkett, J. Kelly, E. Jeffrey, Y. Yang, A. Yu, K. Arya, R. Barends, Z. Chen, B. Chiaro, A. Dunsworth, A. Fowler, C. Gidney, M. Giustina, T. Huang, P. Klimov, M. Neeley, C. Neill, P. Roushan, D. Sank, A. Vainsencher, J. Wenner, T. C. White, and J. M. Martinis, "Qubit compatible superconducting interconnects," Quantum Science and Technology **3**, 014005 (2017).

[37] S. Kosen, H.-X. Li, M. Rommel, D. Shiri, C. Warren, L. Grönberg, J. Salonen, T. Abad, J. Biznárová, M. Caputo, *et al.*, "Building blocks of a flip-chip integrated superconducting quantum processor," Quantum Science and Technology (2022).

[38] G. J. Grabovskij, T. Peichl, J. Lisenfeld, G. Weiss, and A. V. Ustinov, "Strain Tuning of Individual Atomic Tunneling Systems Detected by a Superconducting Qubit," Science **338**, 232 (2012).

[39] L. Faoro and L. B. Ioffe, "Interacting tunneling model for two-level systems in amorphous materials and its predictions for their dephasing and noise in superconducting microresonators," Physical Review B **91**, 014201 (2015).

[40] J. Lisenfeld, A. Bilmes, S. Matityahu, S. Zanker, M. Marthaler, M. Schechter, G. Schön, A. Shnirman, G. Weiss, and A. V. Ustinov, "Decoherence spectroscopy with individual TLS," Scientific Reports **6** (2016).

[41] M. Carroll, S. Rosenblatt, P. Jurcevic, I. Lauer, and A. Kandala, "Dynamics of superconducting qubit relaxation times," arXiv preprint arXiv:2105.15201 (2021).

[42] P. Zhao, T. Ma, Y. Jin, and H. Yu, "Combating fluctuations in relaxation times of fixed-frequency transmon qubits with microwave-dressed states," arXiv preprint arXiv:2203.07857 (2022).

SUPPLEMENTARY MATERIAL

Additional data

The figures on the following pages show the full data set acquired from the optimization routine at various qubit resonance frequencies.

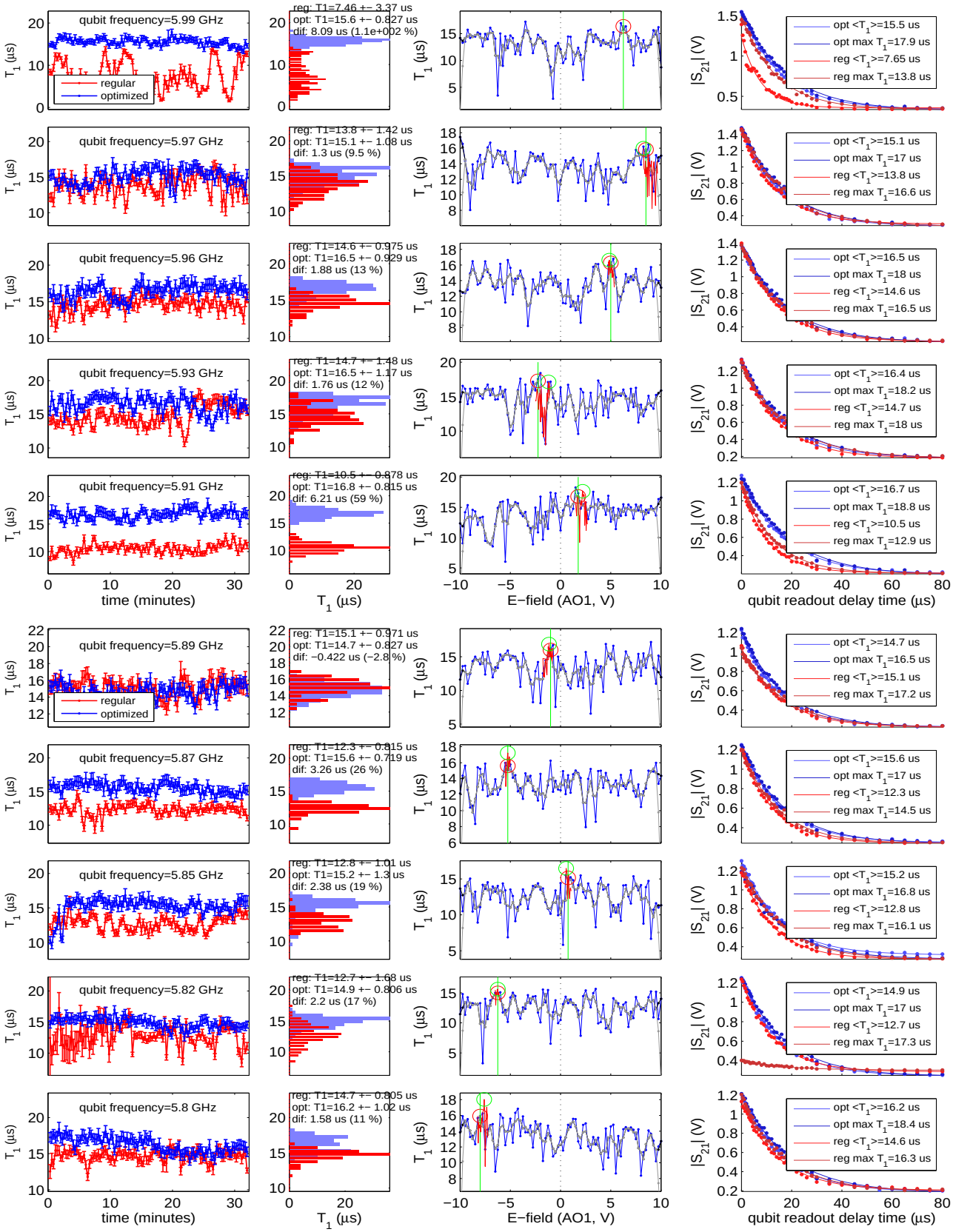

FIG. **S1**. Testing the optimization routine at various qubit frequencies (rows). **Column 1:** T_1 time measured for 30 minutes at zero E-field (red) and optimized E-field (blue). **Column 2:** Histograms of T_1 during 30 minutes for optimized (blue) and zero E-field (red). **Column 3:** T_1 vs. applied E-field to find the optimum E-field (red circle). Data obtained in the second pass is shown in red. **Column 4:** Examples of raw qubit decay curves showing a mean ($< T_1 >$) and maximum (max) T_1 time acquired at optimized (blue) and zero (red) applied E-field.

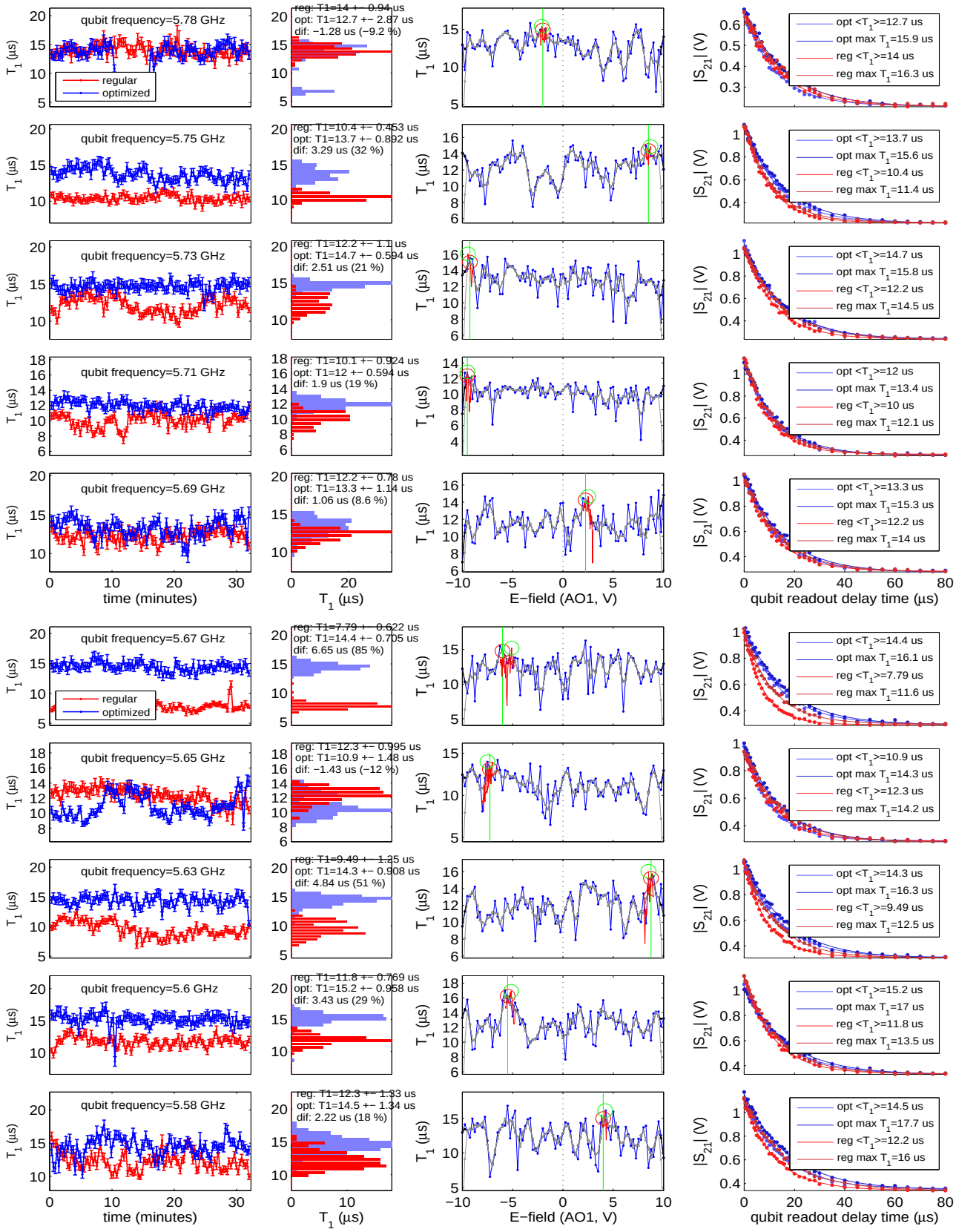

FIG. **S2**. Testing the optimization routine at various qubit frequencies (rows). **Column 1:** T_1 time measured for 30 minutes at zero E-field (red) and optimized E-field (blue). **Column 2:** Histograms of T_1 during 30 minutes for optimized (blue) and zero E-field (red). **Column 3:** T_1 vs. applied E-field to find the optimum E-field (red circle). Data obtained in the second pass is shown in red. **Column 4:** Examples of raw qubit decay curves showing a mean ($< T_1 >$) and maximum (max) T_1 time acquired at optimized (blue) and zero (red) applied E-field.

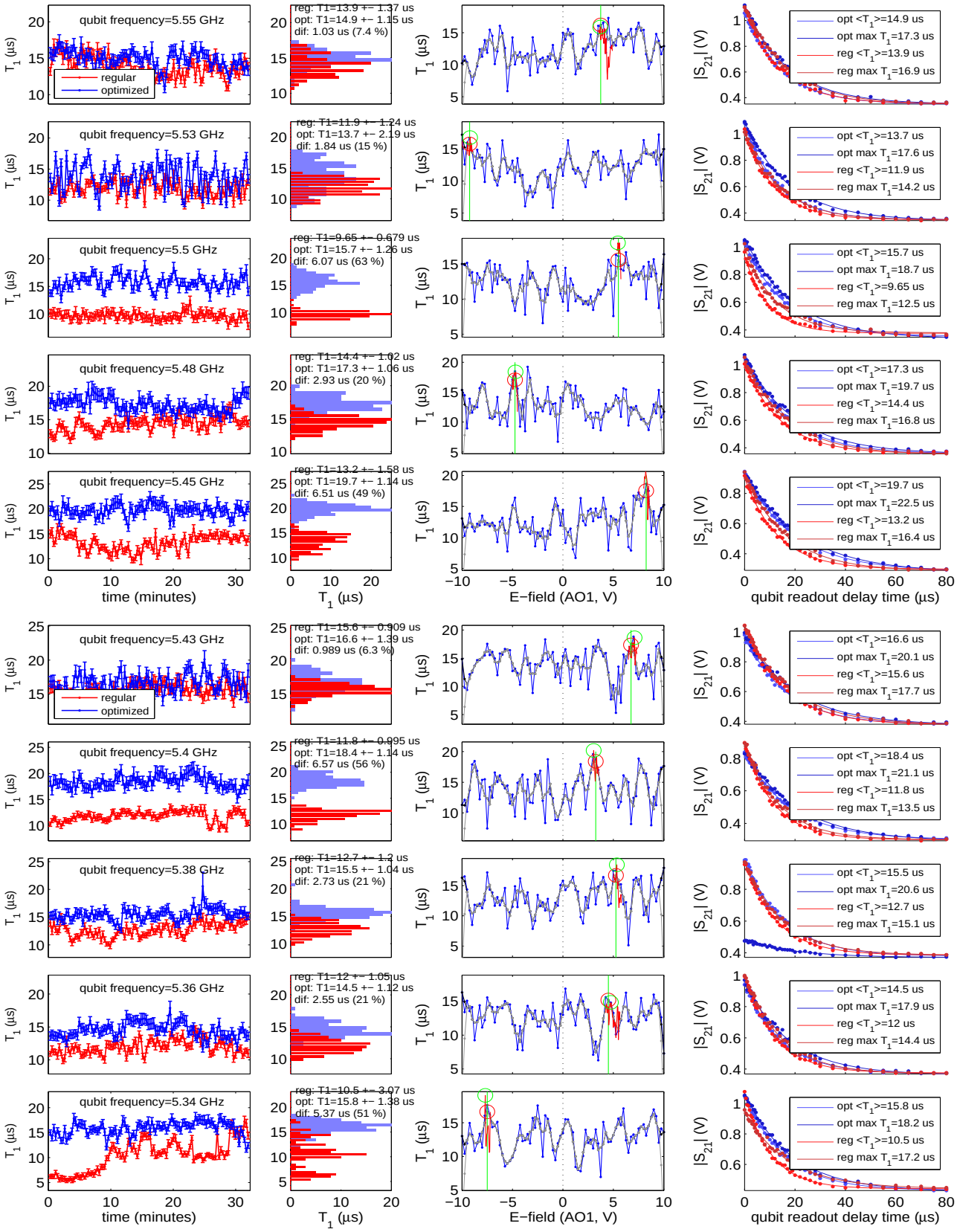

FIG. **S3**. Testing the optimization routine at various qubit frequencies (rows). **Column 1:** T_1 time measured for 30 minutes at zero E-field (red) and optimized E-field (blue). **Column 2:** Histograms of T_1 during 30 minutes for optimized (blue) and zero E-field (red). **Column 3:** T_1 vs. applied E-field to find the optimum E-field (red circle). Data obtained in the second pass is shown in red. **Column 4:** Examples of raw qubit decay curves showing a mean ($< T_1 >$) and maximum (max) T_1 time acquired at optimized (blue) and zero (red) applied E-field.

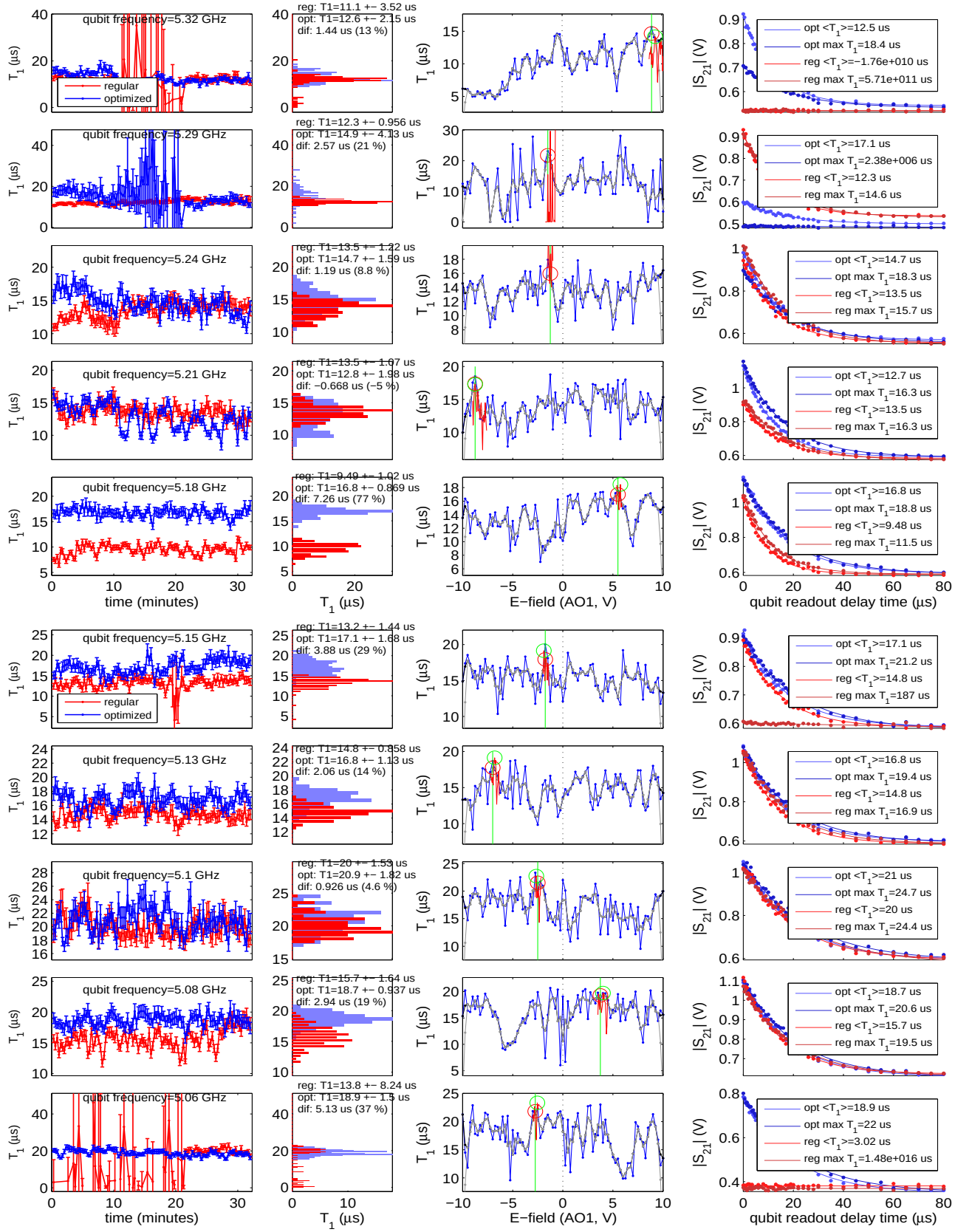

FIG. **S4**. Testing the optimization routine at various qubit frequencies (rows). **Column 1:** T_1 time measured for 30 minutes at zero E-field (red) and optimized E-field (blue). **Column 2:** Histograms of T_1 during 30 minutes for optimized (blue) and zero E-field (red). **Column 3:** T_1 vs. applied E-field to find the optimum E-field (red circle). Data obtained in the second pass is shown in red. **Column 4:** Examples of raw qubit decay curves showing a mean ($< T_1 >$) and maximum (max) T_1 time acquired at optimized (blue) and zero (red) applied E-field.

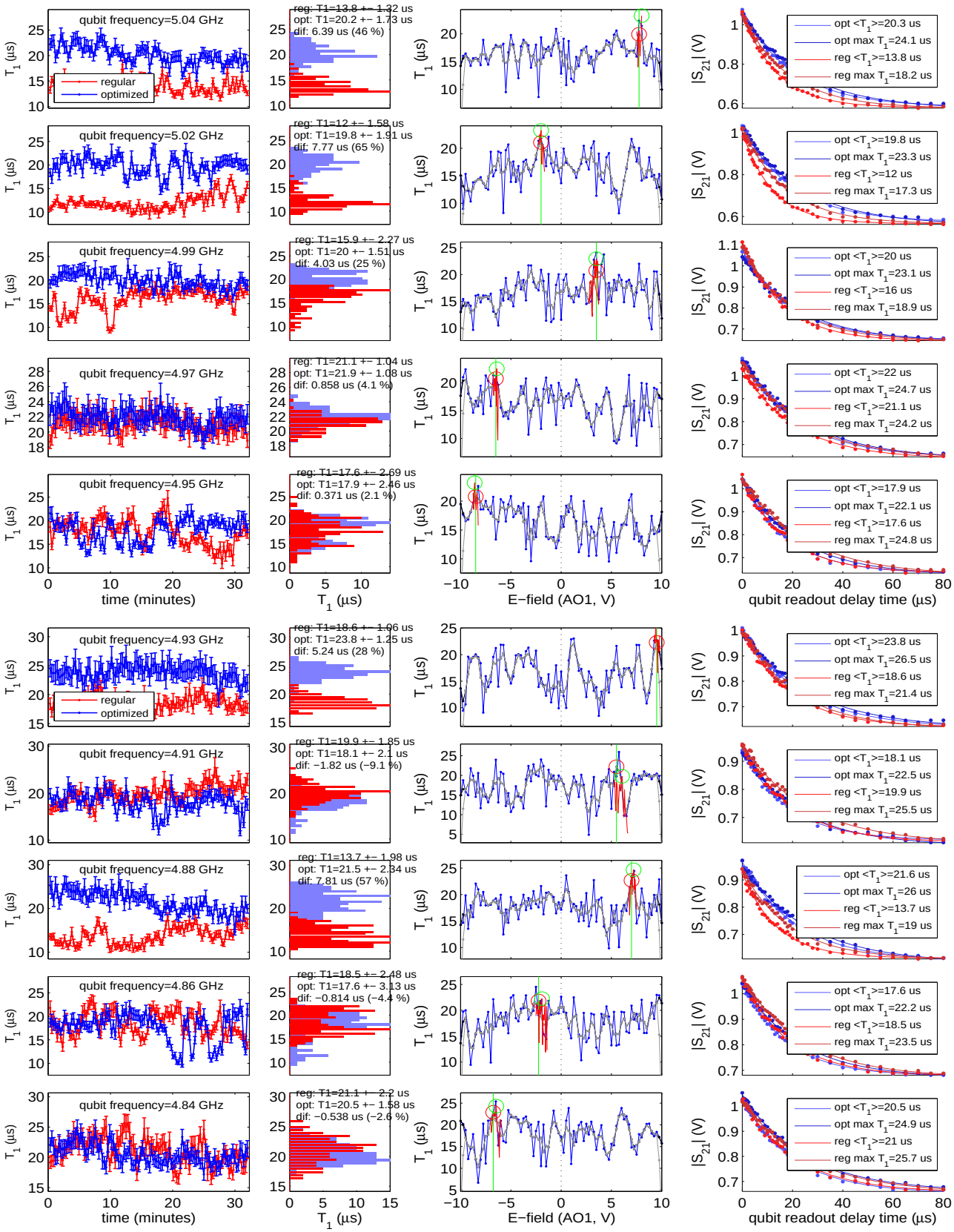

FIG. **S5**. Testing the optimization routine at various qubit frequencies (rows). **Column 1:** T_1 time measured for 30 minutes at zero E-field (red) and optimized E-field (blue). **Column 2:** Histograms of T_1 during 30 minutes for optimized (blue) and zero E-field (red). **Column 3:** T_1 vs. applied E-field to find the optimum E-field (red circle). Data obtained in the second pass is shown in red. **Column 4:** Examples of raw qubit decay curves showing a mean ($< T_1 >$) and maximum (max) T_1 time acquired at optimized (blue) and zero (red) applied E-field.

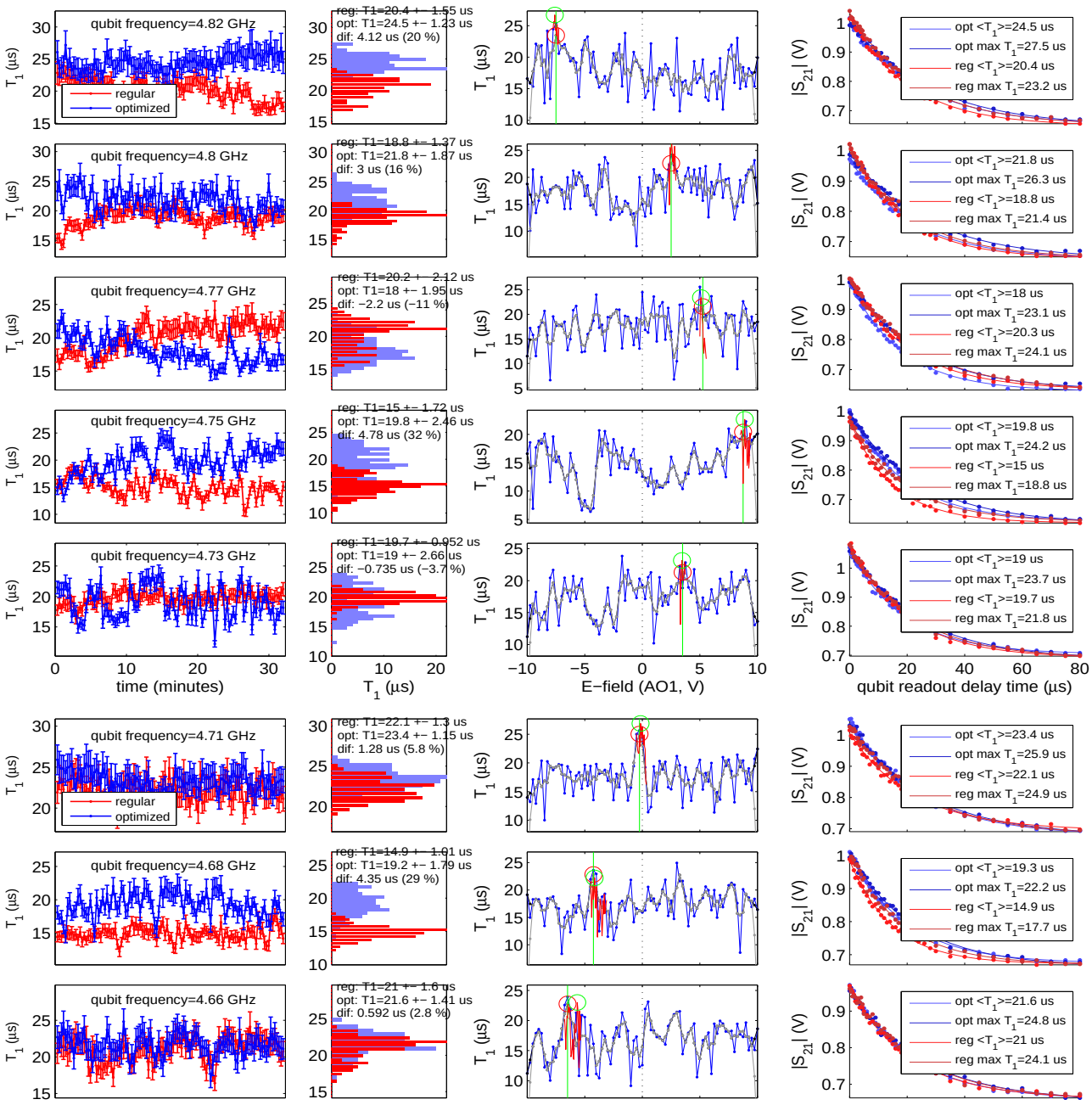

FIG. **S6**. Testing the optimization routine at various qubit frequencies (rows). **Column 1:** T_1 time measured for 30 minutes at zero E-field (red) and optimized E-field (blue). **Column 2:** Histograms of T_1 during 30 minutes for optimized (blue) and zero E-field (red). **Column 3:** T_1 vs. applied E-field to find the optimum E-field (red circle). Data obtained in the second pass is shown in red. **Column 4:** Examples of raw qubit decay curves showing a mean ($< T_1 >$) and maximum (max) T_1 time acquired at optimized (blue) and zero (red) applied E-field.